Non-unit protection method for boundary-component-free MTDC systems using normalized backward traveling waves

Xie, Fan; Liu, Le; Hao, Zhiguo; Wang, Ting; Yang, Songhao; Lekić, Aleksandra; Popov, Marjan

DOI
10.1016/j.ijepes.2024.110370

Publication date
2025

Document Version
Final published version

Published in
International Journal of Electrical Power and Energy Systems

Electrical Power and Energy Systems 164 (2025) 110370

Contents lists available at ScienceDirect

International Journal of Electrical Power and Energy Systems

journal homepage: www.elsevier.com/locate/ijepes

Non-unit protection method for boundary-component-free MTDC systems using normalized backward traveling waves ☆

Fan Xie [a,b,c,1], Le Liu [a,b,1], Zhiguo Hao [a,*], Ting Wang [a], Songhao Yang [a], Aleksandra Lekić [b], Marjan Popov [b]

[a] School of Electrical Engineering, Xi'an Jiaotong University, Xi'an, 710049, China
[b] Faculty of Electrical Engineering, Mathematics and Computer Science, Delft University of Technology, Delft, 2628 CD, The Netherlands
[c] Electric Power Research Institute, China Southern Power Grid, Guangzhou, 510663, China

ARTICLE INFO

Keywords:
Multi-terminal DC system
Traveling wave
Non-unit protection
Vector fitting algorithm
Derivative-free conjugate gradient algorithm

ABSTRACT

The performance of existing protection methods for multi-terminal direct current systems depends on the availability and sizes of boundary components. To overcome the limitation, this paper proposes a non-unit DC line protection method based on the normalized backward traveling waves (BTWs) of the 1-mode voltage. Firstly, traveling wave propagation characteristics are analyzed, and a rationalization approach based on vector fitting is proposed. Next, the analytical expressions of normalized BTWs are derived, with the negative correlation between them and fault distance proved. Then, the derivative-free conjugate gradient algorithm is utilized for amplitude fitting and normalization calculation. Finally, a non-unit protection method using the normalized BTWs is developed. The performance is validated for both electromagnetic transient PSCAD/EMTDC and real-time digital RSCAD/RTDS simulation. The results demonstrate that the proposed method can accurately identify faults with various fault resistances and locations without requiring boundary components and high sampling frequencies, and it is robust against noise disturbances.

1. Introduction

For the integration of renewable energy sources over long distances, modular multilevel converter (MMC)-based high-voltage direct current (HVDC) technology is a proven solution for multi-terminal DC (MTDC) systems. It offers the advantages of no commutation failure, independent active and reactive power control, isolated islands power support, and flexible and adjustable power flow [1].

Large-scale MTDC systems generally utilize long transmission lines, posing high fault probability [2]. Due to the low inertia in MTDC systems, the fault current develops rapidly and exceeds the tolerated over-current capability of power electronic equipment within a few milliseconds [3]. In this regard, protective relays that quickly and accurately identify faults are critical devices [4].

The existing DC line protection approaches can be divided into non-unit and unit methods. Compared with unit methods, the non-unit methods avoid long-distance signal communication and synchronization by using only local measurements [5]. Currently, the non-unit DC line protection methods for MTDC systems primarily use the difference in time/frequency domain between internal and external faults, which originates from the existence of boundary components, e.g., the smoothing reactors and DC filters [6].

The protection methods based on the difference of frequency-domain characteristics mostly use time-domain and frequency-domain analysis tools, such as fast *Fourier* transform, wavelet transform (WT), and empirical modal decomposition, to extract the frequency-domain components of signals in different frequency bands. In [7], the transient voltages are decomposed into multiple detailed coefficients, for fault detection. In [8], the amplitudes of high-frequency voltage TWs are studied, and the WT modulus maximum (WTMM) is utilized to quantify the fault characteristic and to identify different fault scenarios. With accurate time localization, these methods can decompose signals into high/low-frequency components with various layers. However, they all rely on the difference between frequency bands, that are caused by boundary components, and are vulnerable to high-frequency noise [9].

☆ This work was financially supported by the Key Research and Development Program of Shaanxi Province, China (No. 2022GXLH-01-06), China Scholarship Council (No. 202206280073) and the Young Scientists Fund of the National Natural Science Foundation of China (No. 52407142).

* Corresponding author.
E-mail addresses: xiefan@csg.cn (F. Xie), liule@xjtu.edu.cn (L. Liu), zhghao@mail.xjtu.edu.cn (Z. Hao), wang.ting@xjtu.edu.cn (T. Wang), songhaoyang@xjtu.edu.cn (S. Yang), A.Lekic@tudelft.nl (A. Lekić), M.Popov@tudelft.nl (M. Popov).
[1] F. Xie and L. Liu are co-first authors.

https://doi.org/10.1016/j.ijepes.2024.110370
Received 12 July 2024; Received in revised form 16 October 2024; Accepted 6 November 2024
Available online 22 November 2024

The protection methods based on time-domain characteristics mostly use differential and integral calculations to determine fault reference signals, such as the rate of change of voltage (ROCOV) and the ratio of transient voltage (ROTV). The reactor provides a boundary for the DC lines, resulting in an obvious difference between the reactor's ROTV during internal and external faults [10]. As analyzed in [11], the DC voltage discontinues at the boundary components, providing a clear difference between internal and external faults. In [12], a machine-learning-based strategy is proposed, in which the optimal fault detector is chosen from the detector pool containing measured line currents and reactor voltage. However, the time-domain characteristics used in these methods come from the frequency-domain energy distribution differences caused by boundary components. Furthermore, the threshold settings generally depend on numerical simulations [4], and the protection sensitivity is insufficient under high-resistance faults [9].

In addition, non-unit protection can also utilize the distance-based methods, which can identify internal faults from external faults using the distance-dependent features, including TWs [13], resonant frequency [14], and impedance [15]. The impedance-based distance protection method is independent of boundary components. However, it has limited tolerance to fault resistances and an observable detection time due to multiple steps. The other two types of distance-based methods rely on time or frequency information resulting from the refraction and reflection of TWs, which occurs merely when boundary components exist at both line terminals.

To eliminate the dependence on boundary components and overcome the aforementioned shortcomings, this work presents a non-unit DC line protection method for boundary-component-free MTDC systems. Firstly, the paper studies the traveling-wave propagation characteristics and their rationalization approach based on the vector fitting (VF) algorithm. Based on this, the analytical expressions for the normalized 1-mode backward traveling wave (BTW) voltages are derived, which are then used to formulate the non-unit protection method. Then, the amplitudes of BTWs are fitted using the derivative-free conjugate gradient (DF-CG) algorithm, enabling their normalization. Finally, the accuracy validation, robustness analysis, and comparison study are carried out using PSCAD and RTDS.

The main contributions of this work are:

1. The non-unit DC line protection methods based on the normalized BTWs are proposed for boundary-component-free MTDC systems, where existing methods [7–14] are not applicable. The normalized BTWs are analyzed and proven to be distance-dependent and insensitive to fault resistance, guaranteeing that the proposed method correctly identifies internal faults and is robust to fault resistance.
2. The rationalization method for the TW propagation function is proposed using the VF algorithm. This allows for an accurate transformation of the propagation function from the S domain to the time domain, solving the challenges of the detailed time-domain derivation for the normalized BTWs and the analytic pre-setting of the protection thresholds.
3. The amplitude fitting method for TWs is proposed based on the DF-CG algorithm, which implements the normalization of TWs. The DF-CG algorithm eliminates the need to compute the Jacobian matrix for each iteration, thereby improving the poor real-time performance of the protection method due to the use of iterative algorithms, while maintaining the fitting accuracy.

2. Propagation characteristic of TWs

2.1. TW propagation characteristic

When a DC fault occurs, the fault-induced TW voltages U and currents I propagate from the fault point along the lines, which can be expressed as [16]:

$$\begin{cases} U = A_1 e^{-\gamma x} + A_2 e^{\gamma x} = U_\mathrm{f} + U_\mathrm{b}, \\ I = \dfrac{A_1}{Z_\mathrm{C}} e^{-\gamma x} - \dfrac{A_2}{Z_\mathrm{C}} e^{\gamma x} = \dfrac{U_\mathrm{f}}{Z_\mathrm{C}} - \dfrac{U_\mathrm{b}}{Z_\mathrm{C}} = I_\mathrm{f} + I_\mathrm{b}, \end{cases} \tag{1}$$

where x is the location along the line. A_1 and A_2 are the frequency-dependent constants determined by the DC line boundary conditions. $e^{-\gamma x}$ and $e^{\gamma x}$ denote the propagation functions of TWs. γ denotes the frequency-dependent propagation constant, and Z_C denotes the characteristic impedance. U_f and U_b denote the forward traveling wave (FTW) and backward traveling wave (BTW) voltages, respectively. I_f and I_b denote the FTW and BTW currents. We assume that the direction of the FTWs is from the converter station to the line. In contrast, the direction of the BTWs is from the line to the converter station.

The propagation constant γ in (1) is defined as [17]:

$$\gamma = \alpha + \mathrm{j}\beta = \sqrt{(R + \mathrm{j}\omega L)(G + \mathrm{j}\omega C)}, \tag{2}$$

where ω denotes the angular frequency. The frequency-dependent terms R, L, G, and C represent the resistance, inductance, conductance, and capacitance per unit length, respectively. The real part, α, denotes the attenuation constant. The imaginary part, β, denotes the phase constant. They can be expressed as:

$$\alpha, \beta = \frac{\sqrt{2}}{2} \sqrt{\pm \left(RG - \omega^2 LC\right) + \sqrt{\left(R^2 + \omega^2 L^2\right)\left(G^2 + \omega^2 C^2\right)}}. \tag{3}$$

The propagation function $e^{-\gamma l} = e^{-\alpha l} e^{-\mathrm{j}\beta l}$ is used to express the attenuation, distortion, and delay of the initial fault BTWs with a propagation distance l. When substituting the TWs velocity $v = \omega/\beta$, we have:

$$e^{-\gamma l} = e^{-\alpha l} e^{-\mathrm{j}\omega l / v}. \tag{4}$$

Then, substituting $\mathrm{j}\,\omega = s$, the S-domain expression for the propagation function is derived as [18]:

$$e^{-\gamma(s) l} = e^{-\alpha(s) l} e^{-s l / v}, \tag{5}$$

where $e^{-\alpha(s) l}$ denotes the attenuation and distortion of TWs and $e^{-sl/v}$ denotes the delay. The analysis and derivation in this paper focus on the time-domain TWs characteristics, which can be directly extracted from the measured voltages and currents in practice. However, as shown in (3), deriving the time-domain expression of $e^{-\gamma(s) l}$ directly using the inverse *Laplace* transform is complicated, especially deriving expression $e^{-\alpha(s) l}$. Hence, a rationalization method for $e^{-\alpha(s) l}$ is first introduced.

2.2. The rationalization method based on the VF algorithm

With the advantages of reduced iterations, fast computations, high fitting precision, and a wide frequency range, the VF algorithm offers an approach to fit S-domain expression $F(s)$ with the summation of a series of rational fractions [19]:

$$F(s) \approx \sum_{i=1}^{N} \frac{r_i}{s - p_i}, \tag{6}$$

where $i \in \{1, \ldots, N\}$ denotes the sequence number, $N \in \mathcal{Z}^+$ is the positive number of the rational fractions, r_i represents the residue and p_i represents the pole of $F(s)$, respectively.

Assuming that the poles of $F(s)$ are $\bar{p}_1, \ldots, \bar{p}_N$, the auxiliary function $\sigma(s)$ can be constructed as:

$$\begin{bmatrix} \sigma(s) F(s) \\ \sigma(s) \end{bmatrix} \approx \begin{bmatrix} \displaystyle\sum_{i=1}^{N} \frac{r_i}{s - \bar{p}_i} \\ \displaystyle\sum_{i=1}^{N} \frac{\bar{r}_i}{s - \bar{p}_i} + 1 \end{bmatrix}, \tag{7}$$

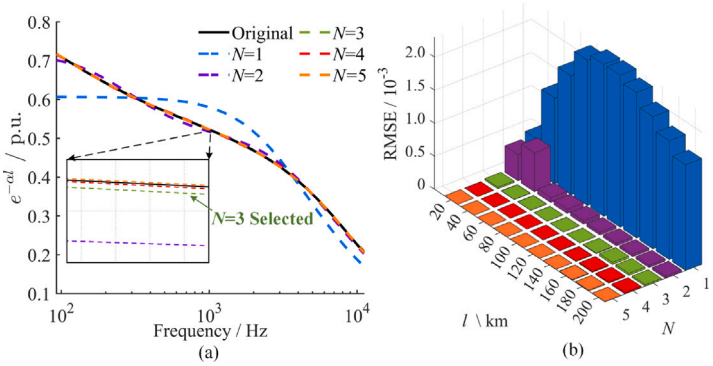

Fig. 1. The fitting accuracy of the VF algorithm: (a) Fitting results; (b) RMSE.

where $r_1, \ldots, r_N$ and $\bar{r}_1, \ldots, \bar{r}_N$ are the residuals of $\sigma(s)F(s)$ and $\sigma(s)$, respectively. They can be obtained by solving the following nonlinear least square (LS) problem:

$$\min \left\| \sigma(s)F(s) - \sum_{i=1}^{N} \frac{r_i}{s-\bar{p}_i} \right\|^2. \tag{8}$$

Then, we can reformulate (8) into:

$$F(s) = \sum_{i=1}^{N} \frac{r_i}{s-\bar{p}_i} - \sum_{i=1}^{N} \frac{\bar{r}_i F(s)}{s-\bar{p}_i} \rightarrow F(s) = \boldsymbol{P} \cdot \boldsymbol{R}^{\mathrm{T}}, \tag{9}$$

where the expressions for $\boldsymbol{R}$ can be solved with the known $F(s)$ and $\boldsymbol{P}$ using the LS method. The $\boldsymbol{P}$ and $\boldsymbol{R}$ are:

$$\begin{cases} \boldsymbol{P} = \left[\frac{1}{s-\bar{p}_1}, \ldots, \frac{1}{s-\bar{p}_N}, -\frac{F(s)}{s-\bar{p}_1}, \ldots, -\frac{F(s)}{s-\bar{p}_N} \right] \\ \boldsymbol{R} = \left[r_1, \ldots, r_N, \bar{r}_1, \ldots, \bar{r}_N \right] \end{cases} \tag{10}$$

With the obtained residuals $r_1, \ldots, r_N$ and $\bar{r}_1, \ldots, \bar{r}_N$ in (9) and (10), the $\sigma(s)F(s)$ and $F(s)$ can be rewritten as:

$$\sigma(s)F(s) = h\frac{\prod_{i=1}^{N}(s-z_i)}{\prod_{i=1}^{N}(s-\bar{p}_i)}, \quad \sigma(s) = \frac{\prod_{i=1}^{N}(s-\bar{z}_i)}{\prod_{i=1}^{N}(s-\bar{p}_i)}, \tag{11}$$

where $z_1, \ldots, z_N$ and $\bar{z}_1, \ldots, \bar{z}_N$ denote zeros of $\sigma(s)F(s)$ and $\sigma(s)$, respectively. h is the amplitude coefficient.

The expression for $F(s)$ can be obtained from (11) as:

$$F(s) = \frac{\sigma(s)F(s)}{\sigma(s)} = h\frac{\prod_{i=1}^{N}(s-z_i)}{\prod_{i=1}^{N}(s-\bar{z}_i)}. \tag{12}$$

As shown in (12), the poles p_i of $F(s)$ are exactly the zeros $\bar{z}_i$ of $\sigma(s)$, which have been calculated in (11).

Replacing $F(s)$ as $e^{-\alpha(s)l}$, it can be fitted as:

$$e^{-\alpha(s)l} \approx \sum_{i=1}^{N} K_i/(1+sT_i), \tag{13}$$

where $K_i = -r_i/p_i$, denoting the attenuation coefficient and $T_i = -1/p_i$, denoting the distortion coefficient.

Thus, by applying the VF algorithm, $e^{-\gamma(s)l}$ is rationalized as:

$$e^{-\gamma(s)l} = e^{-\alpha(s)l}e^{-sl/v} \approx \sum_{i=1}^{N} \frac{K_i}{1+sT_i} e^{-sl/v}. \tag{14}$$

By doing so, the $e^{-\gamma(s)l}$ can be conveniently transformed into the time domain. For validation purposes, the expression $e^{-\alpha(s)l}$ is initially derived in the S domain following (3). Taking $l = 100$ km as an example, $e^{-\alpha(s)l}$ is depicted in Fig. 1(a), utilizing parameter values of R, L, G, and C. Also, the fitting results of $e^{-\alpha(s)l}$ using the VF algorithm are provided in Fig. 1(a). Besides, the accuracy of the fitting is quantified by root mean square error (RMSE), and the results with different values of l and rational fraction number N are presented in Fig. 1(b). The RMSE of the concerned frequency bands can be calculated with:

$$\mathrm{RMSE} = \sqrt{\frac{1}{M}\sum_{j=1}^{M}\left(e^{-\alpha(s_j)l} - \sum_{i=1}^{N}\frac{K_i}{1+s_jT_i}\right)^2}, \tag{15}$$

where j and M denote the sequence number and length, respectively. s_j represents the concerned frequency point.

In (6), the larger N gives better fitting accuracy. However, this also significantly increases the computational complexity from (7) to (12). Therefore, an appropriate N must be selected to balance the fitting accuracy and the computational complexity. As shown in Fig. 1(a), the fitting results for a polynomial of $N \in \{1,2\}$ obviously mismatch the original $e^{-\alpha(s)l}$, while the fitting results of $N \in \{3,4,5\}$ are almost the same as the original $e^{-\alpha(s)l}$. Besides, as shown in Fig. 1(b), for each l, the RMSE decreases as N increases, indicating that the higher values of N lead to higher fitting accuracy. Yet, increasing N from 3 to 4 or 5 does not result in a significant reduction in RMSE (all RMSE less than $1 \cdot 10^{-4}$). Based on these findings, a value of $N = 3$ is chosen in this work, considering the trade-off between the fitting accuracy and computational complexity.

3. Fault analysis for the MTDC system

3.1. Configuration of the MTDC system

Fig. 2 depicts the configuration of the benchmark MTDC system recommended by the Cigre B4.57 working group. The rated DC voltage is ±320 kV. The MMCs utilize half-bridge sub-modules (SMs) and are interconnected by cables through a protection device (R) and a VSC-assisted resonant current (VARC) DC circuit breaker (CB) installed at each terminal [20]. The number of SMs is 200, and each SM capacitor is 15 mF. The bridge equivalent arm inductance and resistance are 5 mH and 0.5 Ω, respectively. These values are the same for each MMC. The rated capacity of each MMC is 1000 MW, and the length of each cable is 200 km.

The $\mathrm{Cable_{MN}}$ is the studied cable, and the $\mathrm{R_{MN1}}$ is the studied protection unit in this work. As such, F1 is the internal fault, F2 is the external fault that occurs at bus N in the positive direction, F3 is the external fault that occurs in the adjacent cable $\mathrm{Cable_{NQ}}$ in the positive direction, and F4 denotes the external fault at bus M in the opposite direction. Notably, unlike typical MTDC systems, boundary components, like smoothing reactors at the cable terminals are not used.

3.2. 1-mode backward traveling waves calculation

When a fault occurs, the initial BTWs generated at the fault point propagate to both terminals and are the first TWs measured by $\mathrm{R_{MN1}}$.

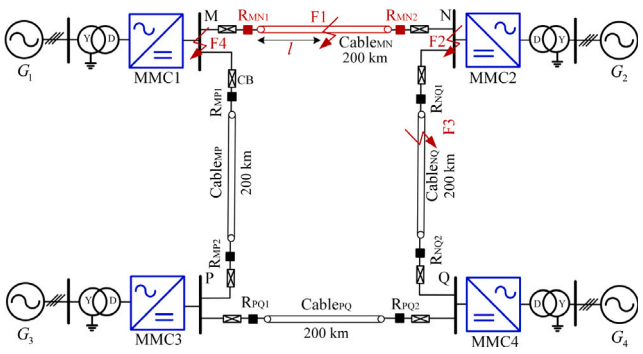

Fig. 2. The configuration of the MTDC system.

Since initial BTWs represent the original characteristics of TWs, they are chosen for the fault analysis.

To eliminate the pole-to-ground and pole-to-pole coupling, the following pole-mode transformation is used [16]:

$$\begin{bmatrix} U_0 \\ U_1 \end{bmatrix} = \frac{1}{\sqrt{2}} \begin{bmatrix} 1 & 1 \\ 1 & -1 \end{bmatrix} \begin{bmatrix} U_P \\ U_N \end{bmatrix}, \begin{bmatrix} I_0 \\ I_1 \end{bmatrix} = \frac{1}{\sqrt{2}} \begin{bmatrix} 1 & 1 \\ 1 & -1 \end{bmatrix} \begin{bmatrix} I_P \\ I_N \end{bmatrix}, \tag{16}$$

where P and N denote the positive and negative poles, respectively, and 0 and 1 denote 0 and 1 modes, respectively.

The 1-mode component, in contrast to the 0-mode component, uses polar lines as its path, making it immune to the grounding conditions. Thus, the following analysis focuses on the 1-mode BTW voltages, of which the S-domain and time-domain expressions are defined as:

$$\begin{cases} U_{b1}(x,s) = \dfrac{U_1(x,s) - Z_{C1} I_1(x,s)}{2}, \\ u_{b1}(x,t) = \dfrac{u_1(x,t) - Z_{C1} i_1(x,t)}{2}. \end{cases} \tag{17}$$

3.3. Fault analysis under internal faults

For internal faults F1, the S-domain expression for the 1-mode BTW voltages $U_{b1,int}(s,l)$ measured at R_{MN1} are [20]:

$$U_{b1,int}(s,l) = \frac{U_{F1}}{s} e^{-\gamma(s)l} \approx \frac{U_{F1}}{s} \sum_{i=1}^{N} \frac{K_i}{1+sT_i} e^{-sl/v}, \tag{18}$$

where the subscript int denotes internal faults, and l denotes the fault distance. U_{F1} is the initial value of the 1-mode TW voltages at the fault point. For a typical positive pole-to-ground (PPTG) fault, negative pole-to-ground (NPTG) fault, and pole-to-pole (PTP) fault, the U_{F1} is determined by [20]:

$$\begin{cases} \text{PPTG: } U_{F1} = \dfrac{-\sqrt{2} Z_{C1} U_r}{Z_{C1} + Z_{C0} + 4R_f}, \\ \text{NPTG: } U_{F1} = \dfrac{-\sqrt{2} Z_{C1} U_r}{Z_{C1} + Z_{C0} + 4R_f}, \\ \text{PTP: } U_{F1} = \dfrac{-\sqrt{2} Z_{C1} U_r}{Z_{C1} + R_f}, \end{cases} \tag{19}$$

where U_r denotes the DC rated voltage. R_f refers to the fault resistance. Z_{C1} and Z_{C0} represent the 1-mode and 0-mode characteristic impedances, respectively.

The expression for the $U_{b1,int}$ in (18) can be rewritten as:

$$U_{b1,int}(s,l) = \left(\frac{A_{int}}{s} - \sum_{i=1}^{N} \frac{K_i U_{F1}}{s + 1/T_i} \right) e^{-st_d}, \tag{20}$$

where $A_{int} = \sum_{i=1}^{N} K_i U_{F1}$ denotes the amplitude of $U_{b1,int}$ and $t_d = l/v$ represents the TWs time delay.

The time-domain expression for $u_{b1,int}(t,l)$ can be obtained using the inverse *Laplace* transform from (20) as:

$$u_{b1,int}(t,l) = \left(A_{int} - \sum_{i=1}^{N} K_i U_{F1} e^{-t/T_i} \right) \varepsilon(t - t_d), \tag{21}$$

where $\varepsilon(t-t_d)$ is a step function with a time delay t_d.

As shown in (21), if F1 occurs, $u_{b1,int}$ contains two components: both step waves and exponential waves. The amplitude of $u_{b1,int}$ is determined by the step waves, and the exponential waves will attenuate to zero. To eliminate the impact of the R_f, $u_{b1,int}$ can be further normalized as the normalized 1-mode BTW voltages $u^*_{b1,int}$ as follows:

$$u^*_{b1,int}(t,l) = \frac{u_{b1,int}(t,l)}{A_{int}} = \left(1 - \sum_{i=1}^{N} \frac{K_i e^{-t/T_i}}{\sum_{i=1}^{N} K_i} \right) \varepsilon(t - t_d). \tag{22}$$

To demonstrate the relationship between $u^*_{b1,int}(t,l)$ and l, $U^*_{b1,int}(s,l)$ is first derived in the S domain from (18):

$$U^*_{b1,int}(s,l) = \frac{U_{b1,int}(s,l)}{A_{int}} = \frac{1}{s} \frac{1}{\sum_{i=1}^{N} K_i} \sum_{i=1}^{N} \frac{K_i}{1+sT_i} e^{-sl/v}. \tag{23}$$

According to (14), when supplementing s, we can obtain $\sum_{i=1}^{N} K_i/(1+sT_i) = e^{-\alpha(s)l}$ and $\sum_{i=1}^{N} K_i = e^{-\alpha(0)l}$. Hence, (23) can be rewritten as:

$$U^*_{b,int}(s,l) = \frac{1}{s} \frac{e^{-\alpha(s)l}}{e^{-\alpha(0)l}} e^{-sl/v} = \frac{1}{s} e^{-[\alpha(s)-\alpha(0)]l} e^{-sl/v}. \tag{24}$$

The derivative of $e^{-[\alpha(s)-\alpha(0)]l}$ with respect to l can be obtained as:

$$\frac{de^{-[\alpha(s)-\alpha(0)]l}}{dl} = -[\alpha(s) - \alpha(0)] e^{-[\alpha(s)-\alpha(0)]l} < 0. \tag{25}$$

It is clear that the derivative $de^{-sl/v}/dl < 0$, and $\alpha(s)$ is higher than $\alpha(0)$ at any frequency (according to (3)). Thus, we have:

$$\frac{dU^*_{b1,int}(s,l)}{dl} < 0, \quad \frac{du^*_{b1,int}(t,l)}{dl} < 0. \tag{26}$$

Based on (26), we can conclude that $u^*_{b1,int}$ decreases as l increases, when internal faults F1 occur.

3.4. Fault analysis under external faults

When F2 occurs DC bus N, the 1-mode BTW voltages $u_{b1,ext}$ (the subscript ext denotes external faults) measured at R_{MN1} match the $u_{b1,int}$ of F1 occurring at the end of $Cable_{MN}$. This is due to their identical faulty circuits when CB impedance is neglected. Thus, the $u_{b1,ext}$ under F2 can be represented by (21), but the fault distance l is the cable length l_c.

When F4 occurs at the DC bus M in the opposite direction, only FTWs are injected into $Cable_{MN}$, and the $u_{b1,ext}$ remain zero until the TWs are reflected to R_{MN1} from the bus N [21].

The $u_{b1,ext}$ of F3, which occurs in $Cable_{NQ}$, will be derived in detail as follows. According to Fig. 3, the S-domain expression for $U_{b1,ext}$ measured at R_{MN1} under F3 can be expressed as [16]:

$$\begin{aligned} U_{b1,ext}(s,l') &= U'_{b1,ext}(s,l'-l_c) e^{-\gamma(s)l_c} \\ &= \frac{2U_{F1}}{s} \frac{Z_{MMC} \parallel Z_{C1}}{Z_{C1} + Z_{MMC} \parallel Z_{C1}} e^{-\gamma(s)l_c} e^{-\gamma(l'-l_c)} \\ &= \frac{U_{F1}}{s} e^{-\gamma l'} - \frac{U_{F1}}{s} \frac{Z_{C1} - Z_{MMC} \parallel Z_{C1}}{Z_{C1} + Z_{MMC} \parallel Z_{C1}} e^{-\gamma(s)l'}, \end{aligned} \tag{27}$$

where the subscript ext denotes external faults. $U'_{b1,ext}$ represent the 1-mode BTW voltages measured by R_{MN2}. l_c is the length of $Cable_{MN}$ and l' denotes the fault distance from R_{MN1} to the fault point of F3 in $Cable_{NQ}$. Z_{MMC} denotes the equivalent impedance of MMC, which contains equivalent resistance R_{eq}, inductance L_{eq} and capacitance C_{eq} [22].

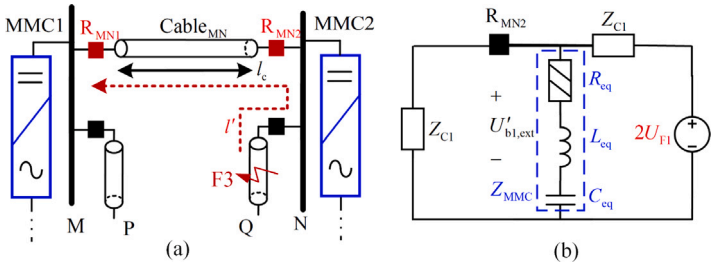

Fig. 3. The system model and equivalent circuit with F3: (a) System model; (b) Equivalent circuit.

Comparing (18) with (27), it is found that $U_{\mathrm{b1,ext}}$ contains a similar part as $U_{\mathrm{b1,int}}$. Therefore, (27) is rewritten as:

$$U_{\mathrm{b1,ext}}(s,l') = U_{\mathrm{b1,int}}(s,l') - U_{\mathrm{b1,add}}(s,l') < U_{\mathrm{b1,int}}(s,l'), \tag{28}$$

where $U_{\mathrm{b1,int}}(s,l')$ is the $U_{\mathrm{b1,int}}$ of F1 with a supposing fault distance l', and $U_{\mathrm{b1,add}}(s,l')$ denotes the difference between $U_{\mathrm{b1,ext}}(s,l')$ and $U_{\mathrm{b1,int}}(s,l')$.

Substituting the expression for Z_{MMC} and the rationalization of $e^{-\gamma(s)l'}$, $U_{\mathrm{b1,add}}$ can be derived as:

$$\begin{aligned} U_{\mathrm{b1,add}}(s,l') &= U_{\mathrm{b1,int}} - U_{\mathrm{b1,ext}} = \frac{U_{\mathrm{F1}}}{s}\frac{Z_{\mathrm{C1}} - Z_{\mathrm{MMC}} \parallel Z_{\mathrm{C1}}}{Z_{\mathrm{C1}} + Z_{\mathrm{MMC}} \parallel Z_{\mathrm{C1}}} e^{-\gamma l'} \\ &\approx \frac{U_{\mathrm{F1}}}{s}\frac{Z_{\mathrm{C1}}}{Z_{\mathrm{C1}} + 2(sL_{\mathrm{eq}} + R_{\mathrm{eq}} + 1/sC_{\mathrm{eq}})} \sum_{i=1}^{N} \frac{K_i}{1+sT_i} e^{-sl'/v}. \end{aligned} \tag{29}$$

The expression in (29) can be rewritten as:

$$U_{\mathrm{b1,add}}(s,l') = \sum_{i=1}^{N}\left(\frac{K_{i1}}{s-s_{i1}} + \frac{K_{i2}}{s-s_{i2}} + \frac{K_{i3}}{s+1/T_i}\right) e^{-sl'/v} \tag{30}$$

where $s_{i1,\,2} = (-R_{\mathrm{eq}}C_{\mathrm{eq}} - Z_{\mathrm{C}}C_{\mathrm{eq}}/2 \pm \sqrt{\Delta})/(2 \cdot L_{\mathrm{eq}}C_{\mathrm{eq}})$, and $\Delta = (R_{\mathrm{eq}}C_{\mathrm{eq}} + Z_{\mathrm{C}}C_{\mathrm{eq}}/2)^2 - 4 \cdot L_{\mathrm{eq}}C_{\mathrm{eq}}$.

Substituting (20) and (30) into (28), $U_{\mathrm{b1,ext}}$ is obtained as:

$$\begin{aligned} U_{\mathrm{b1,ext}}(s,l') &= \left(\frac{A_{\mathrm{ext}}}{s} - \sum_{i=1}^{N}\frac{K_i U_{\mathrm{F1}}}{s+1/T_i}\right) e^{-st'_{\mathrm{d}}} \\ &- \sum_{i=1}^{N}\left(\frac{K_{i1}}{s-s_{i1}} + \frac{K_{i2}}{s-s_{i2}} + \frac{K_{i3}}{s+1/T_i}\right) e^{-st'_{\mathrm{d}}}, \end{aligned} \tag{31}$$

where $A_{\mathrm{ext}} = \sum_{i=1}^{N} K_i U_{\mathrm{F1}}$ is the amplitude of $U_{\mathrm{b1,ext}}$ when an external fault F3 occurs. $t'_{\mathrm{d}} = l'/v$ denotes the time delay.

Using the inverse *Laplace* transform, the time-domain expression for $U_{\mathrm{b1,ext}}$ can be derived as:

$$\begin{aligned} u_{\mathrm{b1,ext}}(t,l') &= \left(A_{\mathrm{ext}} - \sum_{i=1}^{N} K_i U_{\mathrm{F1}} e^{-t/T_i}\right)\varepsilon(t-t'_d) \\ &- \sum_{i=1}^{N}\left(K_{i1}e^{s_{i1}t} + K_{i2}e^{s_{i2}t} + K_{i3}e^{-t/T_i}\right)\varepsilon(t-t'_d). \end{aligned} \tag{32}$$

It is visible that if fault distance l (for internal fault) equals to l' (for external fault), the A_{int} in (20) equals to the A_{ext} in (31). Therefore, according to (28), we can derive:

$$U^*_{\mathrm{b1,ext}}(s,l') < U^*_{\mathrm{b1,int}}(s,l'). \tag{33}$$

where $U^*_{\mathrm{b1,ext}} = U_{\mathrm{b1,ext}}/A_{\mathrm{ext}}$ and $U^*_{\mathrm{b1,int}} = U_{\mathrm{b1,int}}/A_{\mathrm{int}}$.

Then, based on (26) and (33), we can establish the following relationship:

$$\begin{cases} U^*_{\mathrm{b1,ext}}(s,l') < U^*_{\mathrm{b1,int}}(s,l') < U^*_{\mathrm{b1,int}}(s,l_{\mathrm{c}}) < U^*_{\mathrm{b1,int}}(s,l), \\ u^*_{\mathrm{b1,ext}}(t,l') < u^*_{\mathrm{b1,int}}(t,l') < u^*_{\mathrm{b1,int}}(t,l_{\mathrm{c}}) < u^*_{\mathrm{b1,int}}(t,l), \end{cases} \tag{34}$$

where l_{c} is the length of $\mathrm{Cable_{MN}}$, and $l < l_{\mathrm{c}} < l'$.

As shown in (34), $u^*_{\mathrm{b1,ext}}$ of F3 is always smaller than $u^*_{\mathrm{b1,int}}$ of F1 occurring at the end of $\mathrm{Cable_{MN}}$.

Thus, based on the analysis of external faults F2, F3, and F4, the $u^*_{\mathrm{b1,ext}}$ under different scenarios can be summarized as:

$$\begin{cases} \mathrm{F2}: \quad u^*_{\mathrm{b1,ext}}(t,l_{\mathrm{c}}) = u^*_{\mathrm{b1,int}}(t,l_{\mathrm{c}}), \\ \mathrm{F3}: \quad u^*_{\mathrm{b1,ext}}(t,l') < u^*_{\mathrm{b1,int}}(t,l_{\mathrm{c}}), \\ \mathrm{F4}: \quad u^*_{\mathrm{b1,ext}}(t,0) = 0. \end{cases} \tag{35}$$

According to (35), the $u^*_{\mathrm{b1,ext}}$ under any external faults is less than or equal to the $u^*_{\mathrm{b1,int}}$ of internal faults F1. And among them, F2 is the most severe external fault, because the $u^*_{\mathrm{b1,ext}}$ under F2 has the largest value. As such, this characteristic of the normalized 1-mode BTW voltages u^*_{b1} could be used to identify the faulty zone.

4. Non-unit protection method based on normalized backward traveling waves

4.1. The fitting method based on the DF-CG algorithm

In actual HVDC engineering, the sampled u^*_{b1} are not continuous signals but discrete data. To obtain the amplitude of u^*_{b1}, the discrete data are fitted using the parameter fitting method, to solve the nonlinear least squares problem. The DF-CG algorithm is selected for that it converges quickly, requires minimal memory, and does not need to calculate the Jacobian matrix [23].

The error function $\boldsymbol{F}(\boldsymbol{X})$ is defined as:

$$\boldsymbol{F}(\boldsymbol{X}) = u_{\mathrm{b1}}(t_j) - \left(A - \sum_{i=1}^{N_{\mathrm{fit}}} B_i e^{-C_i t_j}\right), \; j \in \{1,2,\ldots,N_{\mathrm{data}}\}, \tag{36}$$

where $\boldsymbol{X} = [A, B_1, \ldots, B_{N_{\mathrm{fit}}}, C_1, \ldots, C_{N_{\mathrm{fit}}}]^T$ denotes the fitted variable. N_{fit} is the size of the fitted variable. N_{data} is the size of sampled data.

Due to the different numbers of exponential waves as given in (21) ($N_{\mathrm{fit}} = N$) and (32) ($N_{\mathrm{fit}} = 4N$), the formulations of $\boldsymbol{F}(\boldsymbol{X})$ vary for $u_{\mathrm{b1,int}}$ and $u_{\mathrm{b1,ext}}$. Here N has been set as 3 in Section 2.2. A fixed N_{fit} is utilized because internal/external fault cannot be identified beforehand in practice. When fitting the u_{b1} under different faults with a fixed number N_{fit} of exponential terms, only B_i and C_i in $\boldsymbol{X}$ are affected, not the amplitude A, as shown in (21) and (32). Since merely A is what we are concerned, the error function (36) with a fixed N_{fit} can be used to normalize the u_{b1} as u^*_{b1}, under different faults. Besides, in this work, we selected $N_{\mathrm{fit}} = N$.

The principle of the DF-CR algorithm is described as:

Step 1: Set the sequence of iterations k (starting from 0), the vector initial value $\boldsymbol{X}_0$, the tolerance error e, the maximum number of iterations $k_{\max}$, and the parameters δ, σ, η, and ρ.

Step 2: Check whether the error $\|\boldsymbol{F}(\boldsymbol{X}_k)\|$ exceeds e. Also, ensure k does not exceed $k_{\max}$. If both conditions are met, continue to the next iteration; otherwise, terminate.

Step 3: Calculate the direction vector $\boldsymbol{d}_k$ and the conjugate coefficient μ_k, according to:

$$\boldsymbol{d}_k = \begin{cases} -\boldsymbol{F}(\boldsymbol{X}_k), & k = 0 \\ -\left(1 + \mu_k \dfrac{\boldsymbol{F}(\boldsymbol{X}_k)^T \boldsymbol{d}_{k-1}}{\left\|\boldsymbol{F}(\boldsymbol{X}_k)\right\|^2}\right)\boldsymbol{F}(\boldsymbol{X}_k) + \mu_k \boldsymbol{d}_{k-1}, & k \geq 1 \end{cases} \tag{37}$$

where $\mu_k = \eta \frac{\|\boldsymbol{F}(\boldsymbol{X}_k)\|}{\|\boldsymbol{d}_{k-1}\|}$, $k \geq 1$.

Step 4: Calculate the trial step λ_k and trial point $\boldsymbol{Y}_k$ using:

$$\begin{cases} \lambda_k = \rho\delta^{m_k}, \\ \boldsymbol{Y}_k = \boldsymbol{X}_k + \lambda_k \boldsymbol{d}_k, \end{cases} \tag{38}$$

where m_k is the smallest non-negative integer, which satisfies:

$$-\boldsymbol{F}(\boldsymbol{X}_k + \rho\delta^{m_k}\boldsymbol{d}_k)^T \geq \sigma\rho\delta^{m_k}\left\|\boldsymbol{d}_k\right\|. \tag{39}$$

Step 5: Calculate $\boldsymbol{X}_{k+1}$ according to:

$$\boldsymbol{X}_{k+1} = \boldsymbol{X}_k - \frac{\boldsymbol{F}(\boldsymbol{Y}_k)^T(\boldsymbol{X}_k - \boldsymbol{Y}_k)\boldsymbol{F}(\boldsymbol{Y}_k)}{\left\|\boldsymbol{F}(\boldsymbol{Y}_k)\right\|^2} \tag{40}$$

Step 6: Increase k, and return to Step 2.

In this work, the values for e, $k_{\max}$, δ, σ, η, and ρ are set to 10^{-5}, 50, 0.5, 0.01, 1, and 1, respectively [23]. Using the iterations from (37)–(40), the amplitude A of u_{b1} is fitted. Then, the normalized 1-mode BTW voltages u^*_{b1} shown as (22) can be obtained for protection design.

4.2. The proposed non-unit protection method

To form a complete protection method, the criteria of start-up, faulty zone identification, and faulty pole identification are studied as follows. Among them, the faulty zone identification criterion is the core, corresponding to the fault analysis in Sections 2 and 3.

4.2.1. Start-up criterion

The start-up criterion is designed based on the absolute variation of the 1-mode voltage Δu_1, which can be expressed as:

$$\left|\Delta u_1(k)\right| > \xi_1, \quad \xi_1 = \mathrm{rel}_1 \cdot \left|\Delta u_1\right|_{\max}, \tag{41}$$

where k denotes the sampling sequence. ξ_1 refers to the threshold. rel_1 represents the reliability factor and is set to 1.2 [20]. $\left|\Delta u_1\right|_{\max}$ is the maximum allowed variation $\left|\Delta u_1\right|$ due to the change of system operation.

4.2.2. Faulty zone identification criterion

According to (35), the $u^*_{b1,ext}$ under external faults are less than or equal to the $u^*_{b1,int}$ of internal faults. In addition, u^*_{b1} is independent of resistance R_f, in contrast to u_{b1}. Therefore, u^*_{b1} is preferred to identify faulty zone, using the criterion as:

$$\mathrm{intg}\_u^*_{b1}(k) = \sum_{j=0}^{M-1} u^*_{b1}(k-j)T_s > \xi_2, \quad \xi_2 = \mathrm{rel}_2 \cdot \mathrm{intg}\_u^*_{b1,\max}, \tag{42}$$

where ξ_2 is the threshold. $\mathrm{intg}\_u^*_{b1,\max}$ denotes the integral of u^*_{b1} when the most severe metallic external fault occurs at the bus N (corresponding to the maximum u^*_{b1}). j denotes the counting order. M is the sample data size within a window of 0.5 ms, ensuring both the detection speed and accuracy. T_s represents the sampling interval. rel_2 is the reliability factor set to 1.2.

4.2.3. Faulty pole identification criterion

The criterion for faulty pole identification is:

$$\begin{cases} \text{PPTG: } \mathrm{intg}\_u_0(k) < -\xi_3, \\ \text{NPTG: } \mathrm{intg}\_u_0(k) > \xi_3, \quad \xi_3 = \mathrm{rel}_3 \cdot \left|\mathrm{intg}\_u_0\right|_{\max}, \\ \text{PTP: } -\xi_3 < \mathrm{intg}\_u_0(k) < \xi_3, \end{cases} \tag{43}$$

where intg_u_0 denotes the integral of 0-mode voltage variation Δu_0. ξ_3 denotes the threshold, and rel_3 denotes the reliability factor set as 1.2. The $\left|\mathrm{intg}\_u_0\right|_{\max}$ refers to the integral determined by the maximum allowed variation Δu_0. Then, intg_u_0 can be obtained according to:

$$\mathrm{intg}\_u_0(k) = \sum_{j=0}^{M-1} \Delta u_0(k-j)T_s. \tag{44}$$

4.3. The auxiliary faulty zone identification criterion

According to (35), when an internal fault F1 occurs at the far end (N) of Cable_{MN}, the normalized 1-mode BTW voltages $u^*_{b1,int}$ measured by the protection R_{MN1} are similar to $u^*_{b1,ext}$ of external faults F2/F3, with the same fault parameters. Hence, the protection range of the proposed non-unit protection method cannot cover the full length of Cable_{MN}, and an auxiliary faulty zone identification criterion is needed in extreme scenarios.

The auxiliary criterion can be written as:

$$P_M(k) = 1 \quad \& \quad P_N(k + k_N - k_M) = 1 \tag{45}$$

where k_M and k_N denote the sampling points when TWs arrive at R_{MN1} and R_{MN2}. P_M and P_N are the integral polarities of the 1-mode current variation Δi_1 measured by R_{MN1} and R_{MN2}, which can be expressed as:

$$P(k) = \begin{cases} 1, & \mathrm{intg}\_i_1 > \xi_4, \\ 0, & \mathrm{intg}\_i_1 \leq \xi_4, \end{cases} \quad \xi_4 = \mathrm{rel}_4 \cdot \left|\mathrm{intg}\_i_1\right|_{\max}, \tag{46}$$

where $\mathrm{intg}\_i_1(k) = \sum_{j=0}^{M-1} \Delta i_1(k-j)T_s$ denotes the integral of Δi_1. ξ_4 denotes the threshold. rel_4 denotes the reliability factor and is set to 1.2. $\left|\mathrm{intg}\_i_1\right|_{\max}$ refers to the integral determined by the maximum allowed Δi_1.

The auxiliary faulty zone identification criterion requires communication between R_{MN1} and R_{MN2}. However, since criterion (45) only requires communicating the polarity P (1 or 0), the economic cost is far less than that for transmitting voltage or current signals.

Besides, this method is primarily demanded when an internal fault occurs near the far end (N) of Cable_{MN} and (42) is not met. In such cases, the time t_M for TWs propagation to R_{MN1} is similar to the sum of the time t_N for TWs propagation to R_{MN2} and the time t_c for data communication between R_{MN1} and R_{MN2} via fiber optic. Time delay t_{delay} can be derived from:

$$t_{delay} = t_N + t_c - t_M = \frac{l_N}{v} + \frac{l_c}{v_c} - \frac{l_M}{v} = \frac{l_c - l}{v} + \frac{l_c}{v_c} - \frac{l}{v} \tag{47}$$

where l_M and l_N represent the distance from the fault point to the terminal M and N, respectively. The TWs velocity v and communication speed v_c are 200 km/ms, and l_c is 200 km.

Consequently, the unit protection causes negligible economic costs and time delays under distant internal faults, which are hard to identify.

The flowchart of the complete proposed protection method is shown in Fig. 4, combining Sections 4.2 and 4.3.

4.4. Threshold setting

According to the operation requirements, each pole's voltage and current fluctuations in the steady state should be lower than 0.05 p.u. [24]. Therefore, for ξ_1, ξ_3, and ξ_4, the maximum values of Δu_1, Δu_0, and Δi_1 are 0.071 p.u. according to Eq. (16). In this case, ξ_1 is set to 0.085 p.u., for the start-up criterion (41). Besides, the integration time windows in (42), (44), and (46) are set to 0.5 ms. Hence, M is 10 with the initial sampling frequency setting to 20 kHz. In this case, both ξ_3 and ξ_4 are set to 0.043 p.u.· ms, for the faulty pole identification criterion (43) and the auxiliary faulty zone identification criterion (45), respectively.

For the faulty zone identification criterion, as summarized in (35), the $u^*_{b1,ext}$ of F2 are closest to the $u^*_{b1,int}$ of F1, so F2 is the external fault scenario where the protection is most likely triggered by mistake. Thus, F2 is the scenario used for setting ξ_2, and $\mathrm{intg}\_u^*_{b1,\max}$ can be analytically calculated as 0.279 when substituting l_c into (22) and using the VF algorithm. In this case, the value of ξ_2 is set to 0.335 p.u.· ms according to (42).

Table 1
Identification results under different scenarios.

Scenario	$\|\Delta u_1\|$ /p.u.	A /p.u.	intg_u^*_{b1} /p.u. · ms	Eq.(42) met ?	Eq.(45) met ?	intg_u_0 /p.u. · ms
F1_PPTG_0%	0.621	−0.621	0.500	Y	Y	−0.324
F1_PTP_0%	1.244	−1.244	0.500	Y	Y	−0.001
F1_PPTG_20%	0.140	−0.522	0.451	Y	Y	−0.259
F1_PTP_20%	0.281	−1.046	0.455	Y	Y	−0.001
F1_PPTG_40%	0.337	−0.477	0.419	Y	Y	−0.250
F1_PTP_40%	0.674	−0.955	0.428	Y	Y	0
F1_PPTG_60%	0.225	−0.440	0.390	Y	Y	−0.215
F1_PTP_60%	0.449	−0.881	0.402	Y	Y	0
F1_PPTG_80%	0.138	−0.406	0.357	Y	Y	−0.184
F1_PTP_80%	0.276	−0.818	0.367	Y	Y	0
F1_PPTG_90%	0.104	−0.386	0.361	Y	Y	−0.171
F1_PTP_90%	0.209	−0.791	0.354	Y	Y	0
F1_PPTG_100%	0.089	−0.363	0.335	N	Y	−0.159
F1_PTP_100%	0.177	−0.766	0.337	Y	Y	0
F2_PPTG	0.088	−0.363	0.322	N	N	/
F2_PTP	0.178	−0.766	0.333	N	N	/
F3_PPTG_10%	0.104	−0.342	0.312	N	N	/
F3_PTP_10%	0.127	−0.704	0.328	N	N	/
F4_PPTG	0.706	0	/	N	N	/
F4_PTP	1.414	0	/	N	N	/

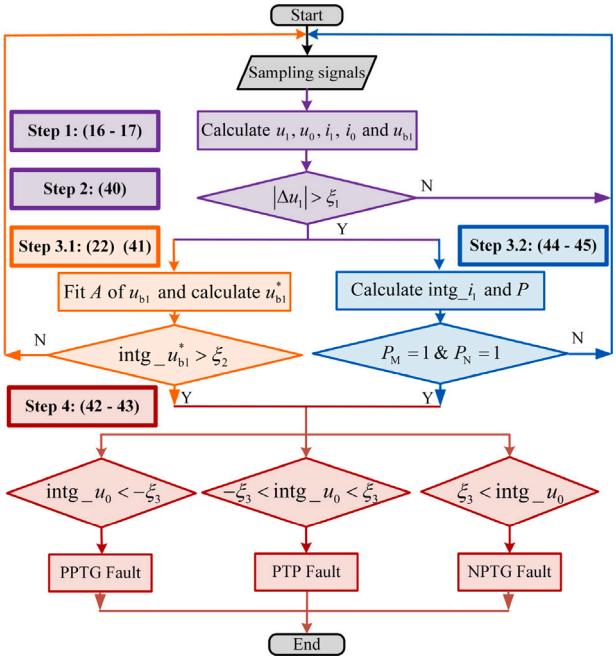

Fig. 4. The flowchart of the protection method.

5. Simulation and analysis in PSCAD

The simulations are carried out using an electromagnetic transient PSCAD/EMTDC platform for the MTDC system depicted in Fig. 2. The R_{MN1} is the studied protection device. For internal faults F1, the R_f is set at values of 0, 10, and 100 Ω. While for external faults F2, F3, and F4, R_f is set to 0 Ω. A larger R_f results in the weak fault characteristic that even fails to satisfy the criterion (41) and to activate protection, and is therefore not considered. All simulated faults initiate at 0 ms and last for 100 ms. The sampling frequency is 20 kHz.

5.1. Simulation analysis

The simulated BTWs u_{b1} and u^*_{b1} of the metallic faults with different fault distances l are provided in Figs. 5 and 6, and the verification results are shown in Table 1. In Fig. 5 and Fig. 6, the numbers in the legend indicate the proportion of l relative to the full length l_c. Here 0% represents F1 occurring at the near end (DC bus M) or F4, while 100% denotes F1 occurring at the far end (DC bus N) or F2.

As shown in Fig. 5, comparing the simulated u_{b1} with the fitted u_{b1}, it is evident that the DF-CG algorithm is effective in fitting the amplitude A of u_{b1}. Additionally, when fitting u_{b1} using the parameter values for e, k_{max}, δ, σ, η, and ρ that are the same as [23], the calculations converge, and the fit is accurate, proving the adaptability and rationality of the parameter values.

In Fig. 5, the mismatch among the waveforms mainly comes from the difference between the actual and selected values of the fitting size N_{fit} for exponential waves in (36). N_{fit} is set to 3 in this work according to Section 4.1. However, when F1 occurs with $l = 0$, only step waves are generated and exponential waves do not exist, so the actual N_{fit} is 0. Besides, when F3 occurs, there are four groups of exponential waves (see (32)), so the actual N_{fit} is $4N = 12$. This mismatch does not affect the fitting of amplitude A, because A is determined by the step waves, rather than the exponential waves in u_{b1}.

As shown in Fig. 6(a), the attenuation and distortion of the simulated u_{b1} are more obvious when distance l increases (with time delays being neglected). With the fitted A, the u_{b1} are normalized to u^*_{b1}, of which the amplitudes are 1, as shown in Fig. 6(b). As the fault distance l increases, the arrival time of u^*_{b1} is delayed, and the waveform becomes smooth, validating the derivations in Sections 3.3 and 3.4.

For all scenarios in Table 1, $|\Delta u_1|$ (minimum is 0.088) exceeds the threshold ξ_1, meeting the start-up criterion in (41), and the protection is activated. In the case of F1, intg_u^*_{b1} decreases as l increases, which is consistent with the findings reported in Section 3.3. Besides, there is no observable difference between the intg_u^*_{b1} of PPTG and PTP faults because the effect of the faulty poles is eliminated when u_{b1} is normalized to u^*_{b1}. For F1, the maximum intg_u^*_{b1} is 0.500 when a metallic fault occurs with a distance $l = 0\% \cdot l_c$. While the minimum intg_u^*_{b1} is 0.335 when a PPTG fault occurs with a long distance $l = 100\% \cdot l_c$. Based on the ξ_2 set in Section 4.4, the intg_u^*_{b1} meets the criterion in (42), when l is less than 90% of the cable length l_c. In contrast, the F1 fault occurring at a longer distance l cannot be identified from external faults by using the proposed non-unit method, as discussed in Section 4.3. However, this challenge can be effectively addressed by the unit protection method described in (45), since the P_M and P_N are the same when F1 occurs, while they differ for F2, F3, and F4. Furthermore, the intg_u_0 (maximum is −0.159) under PPTG faults are less than ξ_3, while the intg_u_0 under PTP faults are near 0, enabling the accurate identification of faulty poles under F1.

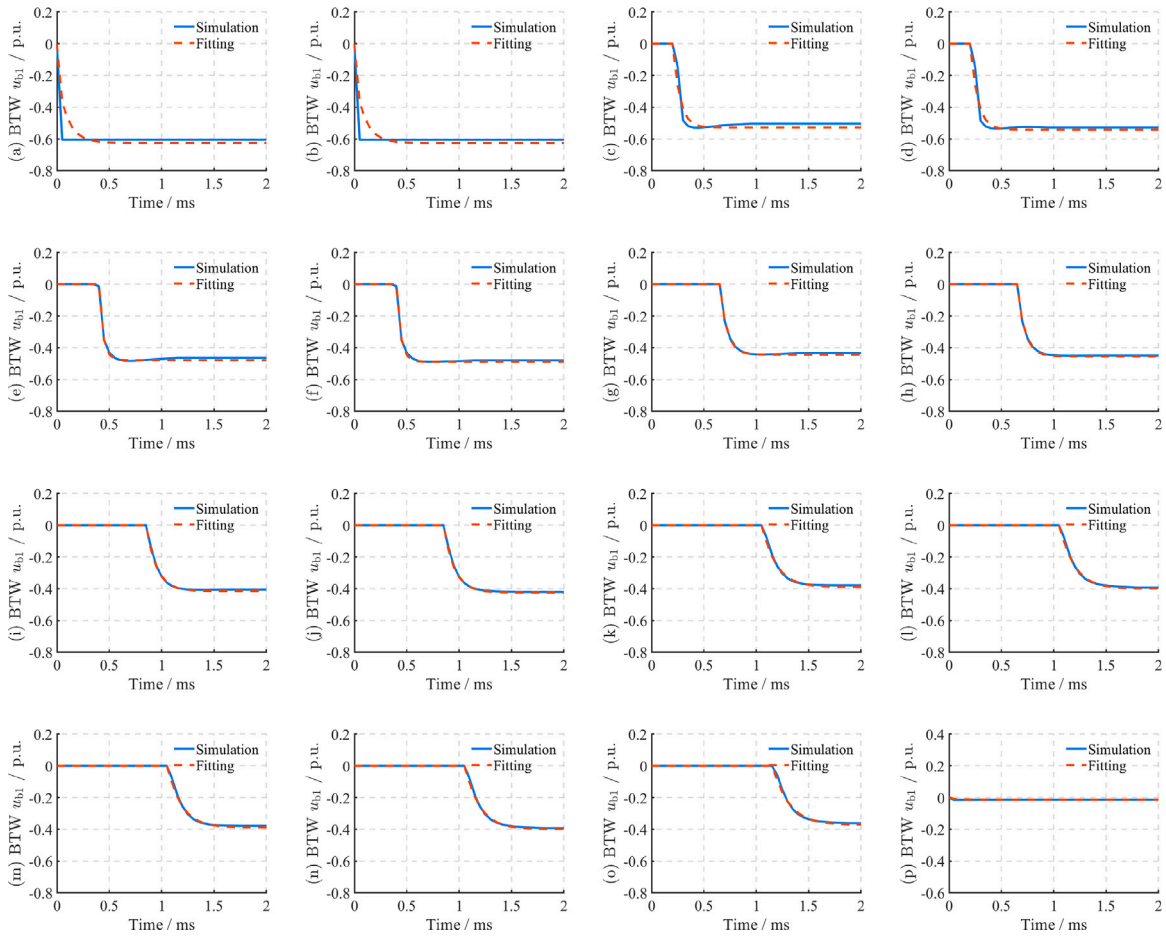

Fig. 5. Simulations and fitting results of BTWs u_{b1} under different scenarios: (a) F1_PPTG_0%; (b) F1_PTP_0%; (c) F1_PPTG_20%; (d) F1_PTP_20%; (e) F1_PPTG_40%; (f) F1_PTP_40%; (g) F1_PPTG_60%; (h) F1_PTP_60%; (i) F1_PPTG_80%; (j) F1_PTP_80%; (k) F1_PPTG_100%; (l) F1_PTP_100%; (m) F2_PPTG; (n) F2_PTP; (o) F3_PTP_10%; (p) F4_PTP.

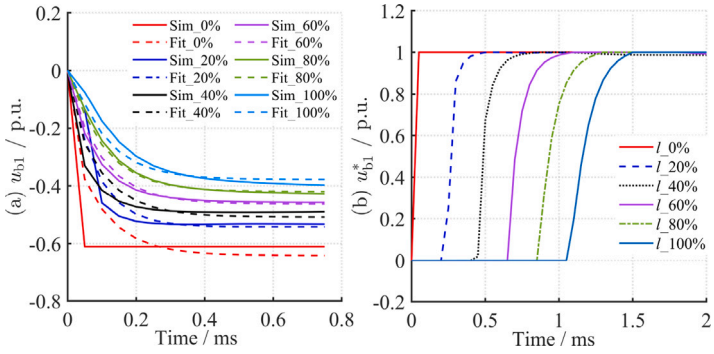

Fig. 6. The simulations of BTWs with different fault distances: (a) Original BTWs u_{b1}; (b) Normalized BTWs u^*_{b1}.

5.2. Robustness analysis

The robustness of the protection method is analyzed when various parameters are altered, and noise is introduced. Due to the space limitations, only the results for the key characteristic, the integral of normalized BTW voltages $\text{intg}\_u^*_{b1}$, are provided.

5.2.1. Robustness against fault resistance

The results for PPTG and PTP faults with various R_f are provided in Fig. 7. In the case of internal faults F1, $\text{intg}\_u^*_{b1}$ decreases as l increases. For each tested value of l, there is no noticeable difference (less than 0.05 p.u.) among the $\text{intg}\_u^*_{b1}$ under F1 with different R_f, as the effect of the R_f is eliminated when u_{b1} is normalized to u^*_{b1}.

For external faults, the maximum $\text{intg}\_u^*_{b1}$ values are 0.322 (PPTG fault) and 0.333 (PTP fault) when F2 occurs at the bus N. Besides, all $\text{intg}\_u^*_{b1}$ for external faults are below the threshold ξ_2. Hence, the protection will not be tripped.

For metallic internal faults F1, $\text{intg}\_u^*_{b1}$ are 0.346 (PPTG fault) and 0.350 (PTP fault) when F1 occurs at 90% of the cable length l_c. Both values meet the criterion in (42). Thus, F1 can be identified as an internal fault when l does not exceed 90% of l_c, which indicates the protection range of the proposed non-unit protection method.

Similarly, when $R_f = 10\,\Omega$, the protection range is 90%, with $\text{intg}\_u^*_{b1}$ values of 0.339 and 0.345. For $R_f = 100\,\Omega$, the protection range is 70%, and the $\text{intg}\_u^*_{b1}$ values are 0.337 and 0.343. The fault F1 occurring at a more distant location must be identified using the

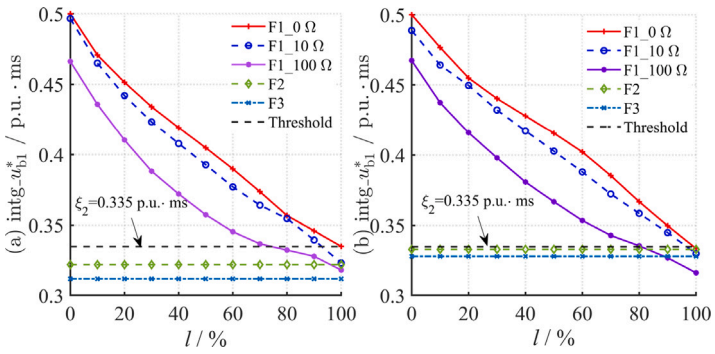

Fig. 7. The integrals of the normalized 1-mode BTW voltages with different fault resistances: (a) PPTG faults; (b) PTP faults.

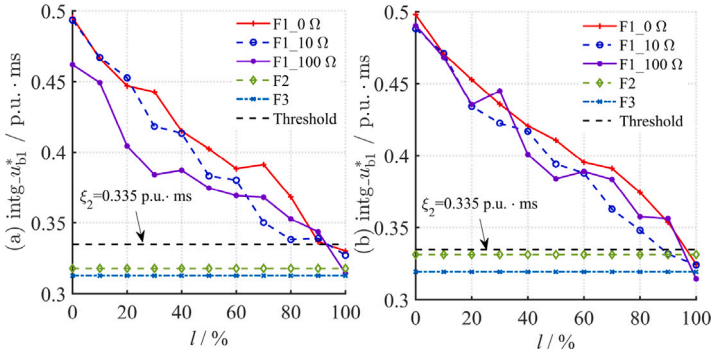

Fig. 8. The integrals of the normalized 1-mode BTW voltages with noise for: (a) PPTG faults; (b) PTP faults.

auxiliary criterion, leading to a trigger delay of up to 0.2 ms ($R_f = 10\,\Omega$) and 0.6 ms ($R_f = 100\,\Omega$), as derived from (47).

5.2.2. Robustness against noise

Noise is one of the main causes of transient voltage and transient current in power transformers and current transformers. The Gaussian white noise (GWN) with a signal-to-noise ratio (SNR) of 35 dB is added to the sampled data. The results under PPTG and PTP faults are provided in Fig. 8.

The GWN is random and notably influences the calculated u^*_{b1}. However, the proposed method identifies faults using the integral of the data over a time window. The impact of random noise can be mitigated. Hence, there is no noticeable difference between the intg_u^*_{b1} values of the faults with the same parameters, when comparing Fig. 8 with Fig. 7.

For external faults F2, the maximum intg_u^*_{b1} values are 0.319 (PPTG fault) and 0.332 (PTP fault). All the intg_u^*_{b1} for external faults are less than the threshold ξ_2. Thus, the protection will not be triggered.

For the internal fault F1 with $R_f = 0\,\Omega$, the values of intg_u^*_{b1} are 0.337 (PPTG fault) and 0.354 (PTP fault), when F1 occurs at 90% of the cable length l_c. Both values meet the criterion in (42). Thus, F1 can be identified as internal faults when l does not exceed 90% of l_c.

Similarly, the protection range is 80% when $R_f = 10\,\Omega$, with intg_u^*_{b1} values of 0.338 and 0.348. While the protection range is 90% when $R_f = 100\,\Omega$, with intg_u^*_{b1} values of 0.344 and 0.356. The internal fault F1, occurring at more distant locations, needs to be identified using the auxiliary criterion, leading to a tripping delay of up to 0.4 ms ($R_f = 10\,\Omega$) and 0.2 ms ($R_f = 100\,\Omega$), as derived from (47).

5.2.3. Robustness under lower sampling frequency

Considering a lower sampling frequency of 10 kHz, the results of PPTG and PTP faults are provided in Fig. 9.

The change in the sampling frequency affects only the intervals between sampling points but not the time-window length. Since the proposed method utilizes the integral in a fixed-length time window, no noticeable difference is observed among the intg_u^*_{b1} values under the faults with the same parameters, when comparing Fig. 9 with Fig. 7.

For external faults, the maximum intg_u^*_{b1} are 0.323 (PPTG fault) and 0.326 (PTP fault) when F2 occurs at the bus N. All the intg_u^*_{b1} of external faults are below the threshold ξ_2. Hence, the protection will not be triggered.

For the internal fault, F1 with $R_f = 0\,\Omega$, intg_u^*_{b1} are 0.345 (PPTG fault) and 0.355 (PTP fault) when F1 occurs at 80% of the cable length l_c. Both values meet the criterion in (42). Thus, F1 can be identified as internal faults when l does not exceed 80% of l_c, which indicates the protection range of the proposed non-unit protection method.

Similarly, the protection range is 80% when R_f is 10 Ω (intg_u^*_{b1} are 0.343 and 0.347), while the protection range is 80% when R_f is 100 Ω (intg_u^*_{b1} are 0.336 and 0.339). The internal fault F1 occurring at a further distance needs to be identified with the auxiliary criterion, leading to a trigger delay of up to 0.4 ms ($R_f = 10\,\Omega$) and 0.4 ms ($R_f = 100\,\Omega$), as derived from (47).

6. Validation and comparison study in RTDS

6.1. Test system in RTDS

To show the effectiveness of the proposed method for different MTDC systems, a detailed three-terminal MMC-HVDC system is modeled in RTDS, as depicted in Fig. 10. The rated DC voltage is ± 200 kV. All three MMCs are modeled using detailed models, requiring three Xilinx Virtex-21 FPGA boards (GTFPGA) for one MMC unit. All cables adopt the frequency-dependent (phase) model. R_{MN1} is the studied protective relay. The sampling frequency is 20 kHz.

6.2. Results analysis

The results are obtained for fault resistance R_f with values 0, 10, and 100 Ω. The results for PPTG and PTP faults are shown in Fig. 11. By following the same threshold setting principle as applied in Section 4.4,

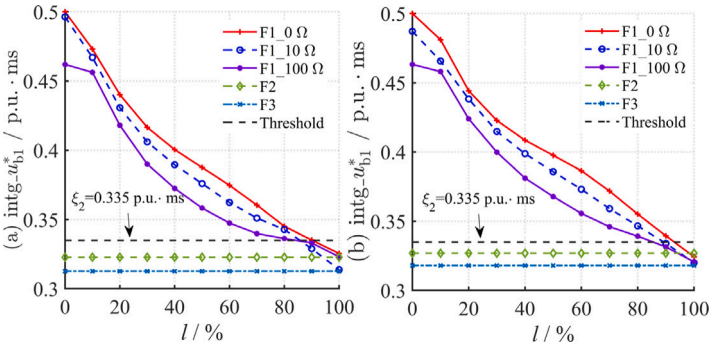

Fig. 9. The integrals of the normalized 1-mode BTW voltages with low sampling frequency: (a) PPTG faults; (b) PTP faults.

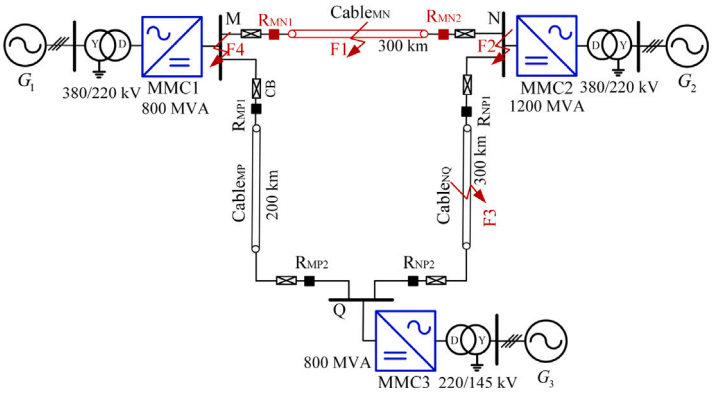

Fig. 10. The configuration of the testing system in RTDS.

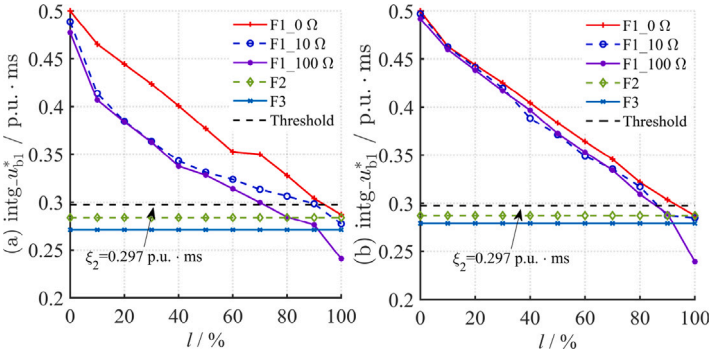

Fig. 11. The integrals of the normalized 1-mode BTW voltages in RTDS: (a) PPTG faults; (b) PTP faults.

the ξ_2 is reset to 0.297 p.u.· ms since the full length of tested cable l_c changes to 300 km in RTDS.

As shown in Fig. 11, for internal fault F1 ($R_f = 0\,\Omega$), intg_u^*_{b1} are 0.304 (PPTG fault) and 0.304 (PTP fault) when F1 occurs at 90% of l_c, and both of them meet the criterion in (42). Thus, F1 can be identified as an internal fault when l does not exceed 90% of l_c, which indicates the protection range of the proposed non-unit protection method.

Similarly, the protection range is 80% when $R_f = 10\,\Omega$ (intg_u^*_{b1} are 0.306 and 0.317), while the protection range is 70% when $R_f = 100\,\Omega$ (intg_u^*_{b1} are 0.300 and 0.334). Internal fault F1 occurring at a further distance needs to be identified by the auxiliary criterion, leading to a trigger delay of up to 0.4 ms ($R_f = 10\,\Omega$) and 0.6 ms ($R_f = 100\,\Omega$), as derived from (47).

6.3. Comparison with other methods

The proposed method is compared with the existing non-unit/unit characteristic-difference- and distance-based methods. The results are presented in Table 2, and parameters are extracted from the cited reference. The detection time refers to the execution time of protection methods. A slash means that the indicator has not been mentioned in the reference. C and O represent cable and overhead lines, respectively. As seen from Table 2, the proposed u^*_{b1}-based method can eliminate the dependence on boundary components, yet the compared methods cannot apply to the boundary-component-free system in principle. Besides, the proposed method has sufficient tolerance against fault resistance (for cables), and its short detection time as well as low sampling frequency requirement can improve identification efficiency and reduce equipment investment.

Furthermore, the existing time-domain characteristic-difference-based methods [10–12] shown in Table 2 are verified for severe conditions and compared with the proposed method. The other methods in Table 2 are based on frequency-domain characteristic difference or impedance, which are different from the type of the proposed method. The verified fault types are remote internal high-resistance PPTG fault (F1) occurring at the 70% of Cable$_{MN}$, and external metallic PTP fault (F2)

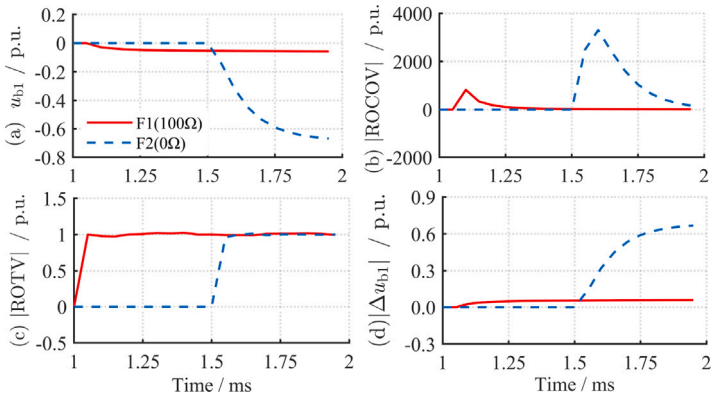

Fig. 12. RTDS results: (a) BTWs of u_{b1}; (b) The absolute value of ROCOV; (c) The absolute value of ROTV; (d) The absolute variation of Δu_{b1}.

Table 2
Parameter comparison with different methods.

Method based on	Rely on boundary?	Sampling frequency	Resistance tolerance	Detection time
u_{b1}^{*} (this work)	No	10 kHz	100 Ω (C)	1 ms
Transient voltage [7]	Yes	10 kHz	300 Ω (O)	2 ms
WTMM [8]	Yes	25 kHz	500 Ω (O)	1.3 ms
ROTV [10]	Yes	10 kHz	400 Ω (O)	1 ms
ROCOV [11]	Yes	100 kHz	200 Ω (O)	1 ms
Variation Δu_{b1} [12]	Yes	100 kHz	200 Ω (O)	1 ms
TW distance [13]	Yes	250 kHz	200 Ω (O)	/
Frequency [14]	Yes	50 kHz	80 Ω (C)	1 ms
Impedance [15]	No	/	100 Ω (O)	25 ms
Curvature [16]	Yes	10 kHz	800 Ω (O)	1 ms
DWT [20]	Yes	100 kHz	500 Ω (C)	2 ms
SWT [21]	Yes	20 kHz	500 Ω (O)	1 ms
WTMM [24]	Yes	250 kHz	400 Ω (O)	2 ms

occurring on bus N. The sampling frequency is 20 kHz, and the data window is 1 ms. The fault resistance (only for F1) is 100 Ω, and the fault inception time is 0 ms. The simulation results are shown in Fig. 12.

As shown in Fig. 12(a), in the abovementioned scenarios, the amplitude of the $u_{b1,ext}$ when F2 occurs obviously exceeds the $u_{b1,int}$ of F1. In contrast, the proposed non-unit method can correctly distinguish F1 from F2, even under severe conditions, as tested in Section 6.2. Nevetherless, the characteristics of F2 are close to F1 (ROTV) or more noticeable than F1 (ROCOV and Δu_{b1}), as shown in Fig. 12(b) to Fig. 12(d). In summary, for the other compared methods, the characteristics of external faults are more obvious than, or similar to, those of internal faults. Hence, it is challenging to set proper protection thresholds, which may result in the protection device misidentifying faults. The comparative analysis shows that the proposed method has low requirements for boundary components and sampling frequency, and has strong robustness against fault resistance.

7. Conclusion

DC transmission line protection is especially challenging for boundary-component-free MTDC grids. This paper proposed a non-unit protection method based on the normalized backward traveling waves of 1-mode voltage. In light of the theoretical analysis and obtained simulation results, we can conclude that:

1. The rationalized approximation of the propagation function achieves its S-to-time-domain transformation and the analytical derivation of the traveling waves in the time domain, enabling the protection thresholds pre-set without simulation.

2. For boundary-component-free MTDC systems, the normalized backward traveling waves under internal faults are proven to decrease as the fault distance increases, and they are more evident than those under any external fault. Besides, this feature can eliminate the effect of fault resistance on the proposed protection method.

3. Simulated PSCAD/RTDS results and comparison with the existing methods validate that the proposed non-unit method does not necessitate boundary components and is robust to high fault resistance (100 Ω for cables), noise disturbance (35 dB), and low sampling frequency (10 kHz). The protection range covers at least 70% of the line length. Besides, the auxiliary faulty zone identification criterion can address the problem of discriminating further internal faults from external faults, leading to a fully protected range.

CRediT authorship contribution statement

Fan Xie: Writing – original draft, Validation, Software, Methodology, Investigation, Data curation, Conceptualization. **Le Liu:** Writing – original draft, Software, Data curation, Conceptualization. **Zhiguo Hao:** Writing – review & editing, Supervision, Funding acquisition. **Ting Wang:** Writing – review & editing. **Songhao Yang:** Writing – review & editing. **Aleksandra Lekić:** Writing – review & editing, Supervision. **Marjan Popov:** Writing – review & editing, Supervision.

Declaration of competing interest

The authors declare that they have no known competing financial interests or personal relationships that could have appeared to influence the work reported in this paper.

Acknowledgments

The first two authors thank TU Delft for providing opportunities to conduct this research at TU Delft in the framework of the CSC program.

Data availability

The authors do not have permission to share data.

References

[1] Li Z, Wang Z, Wang Y, Yin T, Mei N, Yue B, et al. Accurate impedance modeling and control strategy for improving the stability of DC system in multiterminal MMC-based DC grid. IEEE Trans Power Electron 2020;35(10):10026–49. http://dx.doi.org/10.1109/TPEL.2020.2975619.

[2] Zhang C, Song G, Dong X. Non-unit ultra-high-speed DC line protection method for HVDC grids using first peak time of voltage. IEEE Trans Power Deliv 2021;36(3):1683–93. http://dx.doi.org/10.1109/TPWRD.2020.3013021.

[3] Liu L, Shetgaonkar A, Lekić A. Interoperability of classical and advanced controllers in MMC based MTDC power system. Int J Electr Power Energy Syst 2023;148:108980. http://dx.doi.org/10.1016/j.ijepes.2023.108980.

[4] Xiang W, Yang S, Adam GP, Zhang H, Zuo W, Wen J. DC fault protection algorithms of MMC-HVDC grids: Fault analysis, methodologies, experimental validations, and future trends. IEEE Trans Power Electron 2021;36(10):11245–64. http://dx.doi.org/10.1109/TPEL.2021.3071184.

[5] Liu L, Liu Z, Popov M, Palensky P, van der Meijden MAMM. A fast protection of multi-terminal HVDC system based on transient signal detection. IEEE Trans Power Deliv 2021;36(1):43–51. http://dx.doi.org/10.1109/TPWRD.2020.2979811.

[6] Tong N, Lin X, Li Y, Hu Z, Jin N, Wei F, et al. Local measurement-based ultra-high-speed main protection for long distance VSC-MTDC. IEEE Trans Power Deliv 2019;34(1):353–64. http://dx.doi.org/10.1109/TPWRD.2018.2868768.

[7] Li B, Li Y, He J, Wen W. A novel single-ended transient-voltage-based protection strategy for flexible DC grid. IEEE Trans Power Deliv 2019;34(5):1925–37. http://dx.doi.org/10.1109/TPWRD.2019.2910390.

[8] Zhang S, Zou G, Wang C, Li J, Xu B. A non-unit boundary protection of DC line for MMC-MTDC grids. Int J Electr Power Energy Syst 2020;116:105538. http://dx.doi.org/10.1016/j.ijepes.2019.105538.

[9] Sun J, Debnath S, Bloch M, Saeedifard M. A hybrid DC fault primary protection algorithm for multi-terminal HVdc systems. IEEE Trans Power Deliv 2022;37(2):1285–94. http://dx.doi.org/10.1109/TPWRD.2021.3083642.

[10] Liu J, Tai N, Fan C. Transient-voltage-based protection scheme for DC line faults in the multiterminal VSC-HVDC system. IEEE Trans Power Deliv 2017;32(3):1483–94. http://dx.doi.org/10.1109/TPWRD.2016.2608986.

[11] Leterme W, Beerten J, Van Hertem D. Nonunit protection of HVDC grids with inductive DC cable termination. IEEE Trans Power Deliv 2016;31(2):820–8. http://dx.doi.org/10.1109/TPWRD.2015.2422145.

[12] Zhang Y, Tai N, Xu B. Fault analysis and traveling-wave protection scheme for bipolar HVDC lines. IEEE Trans Power Deliv 2012;27(3):1583–91. http://dx.doi.org/10.1109/TPWRD.2012.2190528.

[13] Azizi S, Sanaye-Pasand M, Abedini M, Hasani A. A traveling-wave-based methodology for wide-area fault location in multiterminal DC systems. IEEE Trans Power Deliv 2014;29(6):2552–60. http://dx.doi.org/10.1109/TPWRD.2014.2323356.

[14] Lacerda VA, Monaro RM, Peña-Alzola R, Campos-Gaona D, Coury DV. Nonunit distance protection algorithm for multiterminal MMC-HVdc systems using DC capacitor resonance frequency. IEEE Trans Ind Electron 2022;69(12):12924–33. http://dx.doi.org/10.1109/TIE.2021.3139245.

[15] Liang Y, Huo Y, Zhao F. An accelerated distance protection of transmission lines emanating from MMC-hvdc stations. IEEE J Emerg Sel Topics Power Electron 2021;9(5):5558–70. http://dx.doi.org/10.1109/JESTPE.2021.3058154.

[16] Xie F, Hao Z, Ye D, Yang S, Li C, Dai G, et al. A non-unit line protection method for MMC-HVDC grids based on the curvatures of backward traveling waves. Int J Electr Power Energy Syst 2023;153:109373. http://dx.doi.org/10.1016/j.ijepes.2023.109373.

[17] Snelson JK. Propagation of travelling waves on transmission lines - frequency dependent parameters. IEEE Trans Power Appar Syst 1972;PAS-91(1):85–91. http://dx.doi.org/10.1109/TPAS.1972.293294.

[18] Marti J, Marti L, Dommel H. Transmission line models for steady-state and transients analysis. In: Proceedings joint international power conference athens power tech. vol. 2, 1993, p. 744–50. http://dx.doi.org/10.1109/APT.1993.673895.

[19] Gustavsen B, Semlyen A. Rational approximation of frequency domain responses by vector fitting. IEEE Trans Power Deliv 1999;14(3):1052–61. http://dx.doi.org/10.1109/61.772353.

[20] Liu L, Lekić A, Popov M. Robust traveling wave-based protection scheme for multiterminal DC grids. IEEE Trans Power Deliv 2023;38(5):3117–29. http://dx.doi.org/10.1109/TPWRD.2023.3265748.

[21] Wang T, Yu Z, Xie F, Hao Z, Monti A, Ponci F. Protection of line faults in HVDC grids through convexity detection in backward traveling wave voltages. IEEE Trans Power Deliv 2023;1–17. http://dx.doi.org/10.1109/TPWRD.2023.3286863.

[22] Li R, Xu L, Yao L. DC fault detection and location in meshed multiterminal HVDC systems based on DC reactor voltage change rate. IEEE Trans Power Deliv 2017;32(3):1516–26. http://dx.doi.org/10.1109/TPWRD.2016.2590501.

[23] Abubakar AB, Kumam P. A descent Dai-Liao conjugate gradient method for nonlinear equations. Numer Algorithms 2019;81:197–210. http://dx.doi.org/10.1007/s11075-018-0541-z.

[24] Tang L, Luo S, Shi S. A new differential protection of transmission line based on equivalent travelling wave. IEEE Trans Power Deliv 2016;32:1. http://dx.doi.org/10.1109/TPWRD.2016.2568206.